Quasi-Deterministic Model for Doppler Spread in Millimeter-Wave Communication Systems

Jian Wang, Camillo Gentile, Peter B. Papazian, Jae-Kark Choi, and Jelena Senic

***Abstract*—The most salient feature differentiating millimeter-wave communication systems from their predecessors will be electronically steerable pencilbeam antennas at the transceivers. Due to their extremely narrow beamwidth and the sparse millimeter-wave channel, few multipath components will be captured by the pencilbeams. Although each component has a unique Doppler-frequency shift, the combination of shifts across the detected multipath components captured will give rise to a Doppler spread. The width of the spread is uncertain because, to our knowledge, there are no such measurement results for millimeter-wave systems in open literature to date. To fill this void, we have designed an 83.5-GHz channel sounder that can measure the shift of multipath components in a mobile environment with super-resolution. In this letter, we develop a parameterized model for the Doppler spread by synthesizing the measured frequency shifts through a simulated antenna with variable beamwidth.**

***Index Terms*—Channel coherence time, mobility.**

I. Introduction

In July 2016, the FCC released nearly 11 GHz of spectrum in the 28–73-GHz band for terrestrial wireless communications (an additional 17.7 GHz is currently under review), supporting data rates in excess of 20 Gb/s [1]. Design and planning to define new specifications for millimeter-wave (mmWave) systems are already underway in work groups within the IEEE, 3GPP, and other standards developing organizations. All the while, there is consensus throughout the wireless community that existing channel models in this frequency regime are unreliable, often retrofitted from sub-6-GHz legacy models with mmWave measurements. To date, propagation is not fully understood despite significant efforts, especially in the past two years, to characterize the channel.

The angular properties of the channel are most critical since mmWave transceivers will feature steerable pencilbeam antennas. To characterize these properties, spatial diversity realized through an antenna array is necessary. A brief list of mmWave channel sounders with bandwidth in excess of 500 MHz is [2]–[5]. All implement virtual arrays, that is, a single antenna element is sequentially displaced either through manual or mechanical scanning. Because the total scan takes so long (often hours), only static environment can be evaluated. Our 83.5-GHz channel sounder, on the other hand, features a real physical array and fast electronic switching: A total scan takes only 65 μs such that mobile channels up to a closing speed of 100 km/h [6] can be captured. We are aware of no other mmWave channel sounder capable of this. Consequently, we can collect measurements for Doppler spread, whose accurate characterization is essential to determine channel coherence time and for the design of equalization schemes.

Manuscript received February 1, 2017; revised April 24, 2017; accepted May 10, 2017. Date of publication May 18, 2017; date of current version August 7, 2017. *(Corresponding author: Camillo Gentile.)*

J. Wang, C. Gentile, and J.-K. Choi are with the Wireless Networks Division, National Institute of Standards and Technology, Gaithersburg, MD 20899 USA (e-mail: jian.wang@nist.gov; camillo.gentile@nist.gov; jaekarkchoi@gmail.com).

P. B. Papazian and J. Senic are with the RF Technology Division, National Institute of Standards and Technology, Boulder, CO 80305 USA (e-mail: peter.papazian@nist.gov; jelena.senic@nist.gov).

Color versions of one or more of the figures in this letter are available online at http://ieeexplore.ieee.org.

Digital Object Identifier 10.1109/LAWP.2017.2705578

II. Channel Measurements

Our 83.5-GHz channel sounder features an omnidirectional antenna at the transmitter (TX) and a 16-element antenna array at the receiver (RX). The octogonal array enables angle-of-arrival (AoA) discrimination in both azimuth and elevation. The TX signal is a pseudorandom-noise sequence with 1-GHz chip rate, sustaining multipath-component (MPC) resolution better than 1 ns when super-resolution techniques are employed. A single acquisition consists of 128 time samples of the channel with sample rate $\Delta t = 0.52$ ms, corresponding to a maximum measureable Doppler shift $|\Delta f|_{\max} = \frac{1}{2\Delta t} = 961.5$ Hz. Each time sample consists of 16 complex impulse responses between the TX and each RX element. The samples are processed collectively to extract the channel MPCs. The measured Doppler shift is the rate of the MPC phase rotation over the samples. Exhaustive details of the system and the MPC extraction method are available in [6].

For results in this letter, a total of 24 acquisitions were collected in line-of-sight (LOS) conditions in a basement environment. The dimensions of the room are $7 \times 7 \times 6$ m^3. The TX was mounted on a fixed tripod at 1.6 m height, while the RX was mounted on a mobile robot, also at 1.6 m. The laser-guided navigational system of the robot reported the varying position, heading, and speed of the robot at each acquisition. The robot accelerated from 0 km/h to a maximum speed of 3 km/h or 278 mm/s (reported with a granularity of 1 mm/s). The azimuth AoA was reported in reference to the robot heading ($\theta = 0°$), and the elevation AoA in reference to the ground plane.

III. Quasi-Deterministic Model

The IEEE 802.11ay task group [1] as well as other industry consortia (e.g., METIS2020 [7], MiWEBA [8], mmMAGIC [9]) have subscribed to map-based channel propagation models for mmWave systems, such as the quasi-deterministic (QD) model [10]. In the QD model, the direct path and reflected paths only are considered (as diffraction has been shown to be much less significant in the mmWave bands [11]). The direct path is completely deterministic: Its delay and AoA are computed from

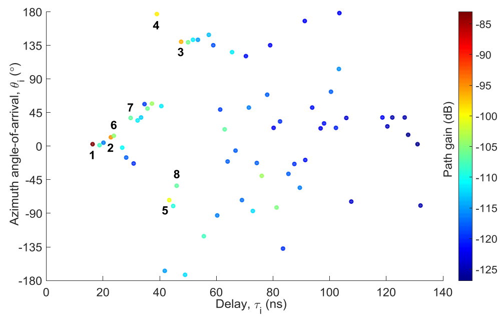

Fig. 1. Power angle-delay profile of a single acquisition. Each multipath component (MPC) is indexed according to (color-coded) path gain, delay, and AoA (only azimuth shown here). The boldface numbers indicate the top eight cursors ranked according to path gain.

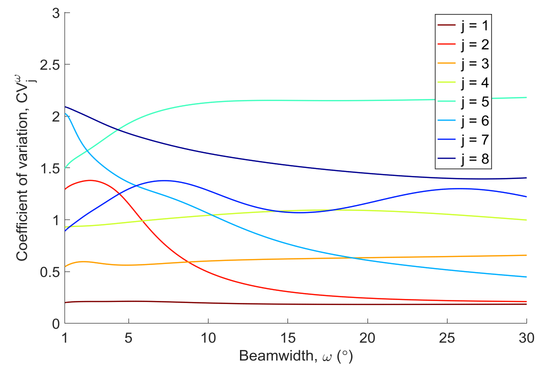

Fig. 2. Coefficient of variation for the top eight cursors of the example measurement in Fig. 1.

the geometry of the TX and RX, and its path gain from Friis transmission equation in LOS. Similarly, specular reflections are also deterministic given the map of the environment (and any reflection loss). Each specular reflection gives rise to scattering of the incident wave into a dominant MPC, also known as cursor, and weaker diffuse components clustered around it.

From a single acquisition, N MPCs are excised, and the ith MPC is classified according to path gain (PG_i), delay (τ_i), azimuth (θ_i) and elevation (ϕ_i) AoA, and Doppler shift (Δf_i). Fig. 1 shows the power angle-delay profile of an example acquisition. The eight cursors identified were ranked in terms of path gain and labeled from $j = 1, \ldots, 8$ accordingly. The direct path is the strongest, and the other seven originate from ceiling, ground, or wall reflections, each surrounded by weaker diffuse reflections. The nondeterministic property of the model describes the statistics of the clustered scattering. Between five and eight cursors were identified in each acquisition.

In mmWave systems, ideally the RX antenna will align its beams along the AoAs of the cursors. In other words, the jth beam will be centered at the azimuth and elevation $(\boldsymbol{\theta}_j, \boldsymbol{\phi}_j)$ of the jth cursor. In this letter, we simulate antennas beams of varying beamwidth. A practical assumption is that the beam will have a Gaussian antenna pattern

$$G_j^\omega(\theta, \phi) = e^{-\frac{(\theta - \boldsymbol{\theta}_j)^2 + (\phi - \boldsymbol{\phi}_j)^2}{\omega^2 / \ln 4}} \tag{1}$$

where ω denotes the half-power beamwidth. The wider the beamwidth, the greater the contribution of the diffuse components. Because each MPC will have a unique Doppler shift, the sum over the detected components will give rise to a Doppler spread. The spread will depend not only on the beamwidth, but also on the strength of the cursor with respect to the diffuse components. In the QD model, this relative strength is gauged through the K-factor

$$K_j^\omega = \frac{\max_i \left[\mathrm{PG}_i \cdot G_j^\omega(\theta_i, \phi_i)\right]}{\sum_{i=1}^N \mathrm{PG}_i \cdot G_j^\omega(\theta_i, \phi_i) - \max_i \left[\mathrm{PG}_i \cdot G_j^\omega(\theta_i, \phi_i)\right]}. \tag{2}$$

Whereas the cursor enjoys the full gain of the antenna, the diffuse components absorb a roll-off gain in proportion to the distance from the cursor in the angle space.

IV. Doppler Spread Model

In this section, we develop a model for the Doppler spread that is linked to the QD model. The parameters that link the two are the cursors' K-factors and their AoAs.

The root-mean-square Doppler spread as seen by the jth beam in a single acquisition is defined as

$$\sigma_j^\omega = \sqrt{\frac{\sum_{i=1}^N \mathrm{PG}_i \cdot G_j^\omega(\theta_i, \phi_i) \cdot \left(\Delta f_i - \mu_j^\omega\right)^2}{\sum_{i=1}^N \mathrm{PG}_i \cdot G_j^\omega(\theta_i, \phi_i)}} \tag{3}$$

where

$$\mu_j^\omega = \frac{\sum_{i=1}^N \mathrm{PG}_i \cdot G_j^\omega(\theta_i, \phi_i) \cdot \Delta f_i}{\sum_{i=1}^N \mathrm{PG}_i \cdot G_j^\omega(\theta_i, \phi_i)} \tag{4}$$

is the mean Doppler shift of the beam. In order to aggregate data across the acquisitions, we compute the coefficient of variation

$$\mathrm{CV}_j^\omega = \frac{\sigma_j^\omega}{|\mu_j^\omega|} \tag{5}$$

which is a normalized spread that accounts for the varying mean of the data points.

Fig. 2 displays CV_j^ω versus ω for the eight cursors of the example acquisition in Fig. 1. The data points were generated for $1^\circ \leq \omega \leq 30^\circ$. For the direct path ($j = 1$), the normalized spread remains flat with beamwidth. This is because its K-factor remains large, from 25.6 dB at $\omega = 1^\circ$ to 11.2 dB at $\omega = 30^\circ$. Hence, admitting more diffuse paths has little effect. The case is different for the second cursor corresponding to the ceiling bounce with estimated azimuth angle in line with the direct path (but with higher elevation angle): For narrow beamwidths, the coefficient begins to increase; hence admitting more diffuse components is indeed noticeable. However, beyond the peak at *breakpoint* $\omega_2 = 2.6^\circ$—a breakpoint ω_j is defined at the first peak[1] in the CV_j^ω profile—the coefficient begins to drop. This is because the second beam starts to admit the direct path as well, i.e., interbeam interference comes into play. The normalized spread continues to decrease and eventually approaches that of the direct path because the direct path is so dominant with respect to the ceiling bounce.

As the width of beam 3 increases, its normalized spread rises mildly with ω; eventually, the beam captures cursor 4 nearby, yet no interbeam interference is experienced because cursor 3 is stronger than cursor 4. Conversely, beam 4 does experience interference with cursor 3 at $\omega_4 = 17.8^\circ$ after the initial rise in spread. However, since the two cursors are comparable in strength (–98.0 versus –99.5 dB), the drop-off is

[1]The peak is at least 5% higher than neighboring values. The 5% threshold filters out any fluctuations in the profile due to estimation error in the MPC parameters.

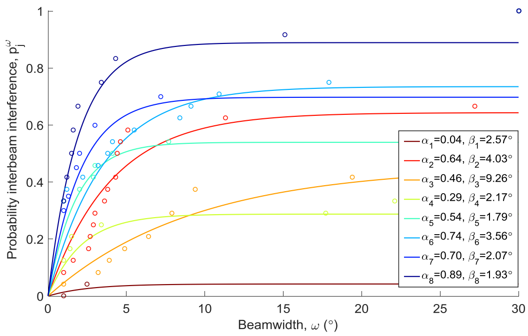

Fig. 3. Probability of interbeam interference for the eight beams. The circles indicate data points computed from the measurements while the lines indicate the model in (6) fits to the points. The model parameters for the individual cursors appear in the legend.

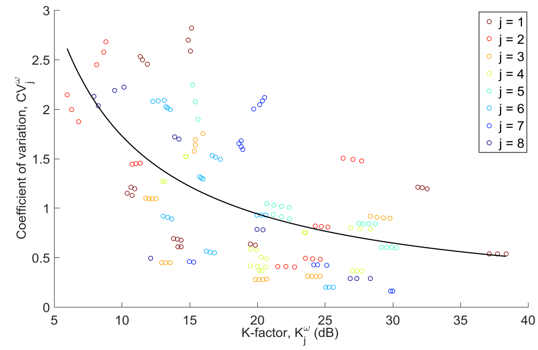

Fig. 4. Plots shows that the *K*-factor is a good indicator for the coefficient of variation.

mild. Similarly, interference for beams 5–8 depends both on the angular separation between the cursors and on their relative strengths. The varying breakpoints for the beams are: $\omega_5 < 1^\circ$ and $\omega_6 < 1^\circ, \omega_7 = 7.3^\circ$ (beam 7 even has two peaks), and $\omega_8 > 30^\circ$.

In order to quantify interbeam interference, we calculate the probability p_j^ω of a breakpoint for the beams over the 24 acquisitions. The probability expresses the likelihood of interference occurring at a specific beamwidth. For each j, both the measured data points (circles) and the parametric model below fit to the points are shown in Fig. 3:

$$p_j^\omega = \alpha_j \cdot \left(1 - e^{-\frac{\omega}{\beta_j}}\right), \;\; \omega \leq 30^\circ. \tag{6}$$

The parameters (α_j, β_j) are displayed in the figure legend. In general, the asymptotic probability α_j increases with j while the decay constant β_j decreases, meaning that interference is more likely as the cursor strength decreases. The main exception is for $j = 2$—the second is always the ceiling bounce across the acquisitions—since its beam is closely aligned with the direct path.[2]

A. Normalized Model

The model we develop for Doppler spread assumes no interbeam interference. Since it was observed that the highest-ranking cursor of any mutual interferers will experience little to no interference even when present, the model also covers this case; the behavior of the spread for the lower ranking cursors, however, is complex since the signal will be distorted and hence difficult to equalize. That is why, in order to mitigate interference, mmWave systems will sound the channel in advance of data transmission, hence modeling this behavior is less relevant.

Through (6), we can determine the likelihood of interference given the system beamwidth. However, the beamwidth alone is insufficient to predict the Doppler spread. For instance, in Fig. 2, the normalized spread remains almost constant across ω for $j = 1$, while for $j = 3$, it is more than twice as large as for $j = 1$ at $\omega = 1^\circ$ and then increases almost monotonically. A better indicator for the spread is the *K*-factor, K_j^ω, in (2). This is because it also accounts for the relative power of the cursor with respect to the diffuse components in the beam. In fact, Fig. 4 plots CV_j^ω versus K_j^ω for the cursors across the 24 acquisitions.[3]

What is interesting to notice is that there is no aggregation of points based on the cursor rank j. This suggests that the normalized spread is independent of cursor rank, simplifying our model for the coefficient of variation, $\widehat{\text{CV}}_j^\omega$. Hence, to derive the model, we fit a single curve (black) to all the points in the plot in Fig. 4. The parametric equation for the model is

$$\widehat{\text{CV}}_j^\omega = \frac{20.8 \text{ dB}}{\hat{K}_{j\,\text{dB}}^\omega + 2.0 \text{ dB}} + \mathcal{N}(0,\ 0.51) \tag{7}$$

where $\hat{K}_{j\,\text{dB}}^\omega$ is the *K*-factor in decibels and $\mathcal{N}$ denotes the zero-mean Gaussian distribution with standard deviation 0.51.[4]

B. Absolute Model

The coefficient of variation is only a relative metric, and what is needed for system design, rather, is the absolute Doppler spread. To this end, consider first the conventional model for Doppler shift [12]:

$$\widehat{\Delta f}_i = \frac{v}{c} \cos \hat{\theta}_i \cdot f_c \tag{8}$$

where v denotes the RX speed, c the speed of light, $\hat{\theta}_i$ the model AoA, and f_c the center frequency of operation. Note that the shift is just a function of azimuth (not elevation) since the robot only moves in the azimuthal plane. Fig. 5 plots the measured shift Δf_i versus the model shift $\widehat{\Delta f}_i$ for the cursors across the acquisitions. The plot confirms the one-to-one correspondence between the two (indicated by the black line). Any deviation from the line can be attributed to estimation errors in either Δf_i or $\widehat{\Delta f}_i$. Because the phase stability of our system is extremely accurate, the major source of error in Δf_i is likely due to quantization, i.e., the measured Doppler is bound to 128 discrete points (number of time samples). Conversely, the model shift is computed from the tracked speed of the robot and the measured θ_i. Since the tracked speed of our system is also very accurate, the major source of error in $\widehat{\Delta f}_i$ lies in the estimation of θ_i. While useful for validation, in practice the model shift is given from the QD model parameters for the speed and the AoA.

[2]The ground bounce is rarely detected due to the RX-antenna boresight pointed upwards.

[3]To exclude interbeam interference, only values before the breakpoints are considered.

[4]Due to the Gaussian distribution, negative generated values of $\widehat{CV}$ should be truncated to 0.

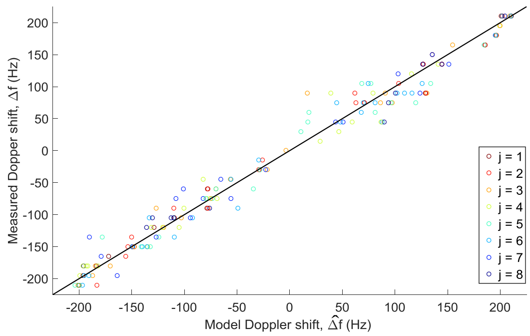

Fig. 5. One-to-one correspondence between the measured and model Doppler shifts of the top eight cursors. The wide range of shifts stems from the varying position, heading, and speed of the robot across the 24 acquisitions in the campaign.

Given the equivalence between the measured and model Doppler shifts, we can substitute the parameterized expression in (8) for the measured value in (4), yielding the model mean Doppler shift of the beam

$$\hat{\mu}_j^{\omega} = \frac{\sum_{i=1}^{\hat{N}} \widehat{\mathrm{PG}}_i \cdot G_j^{\omega}\left(\hat{\theta}_i, \hat{\phi}_i\right) \cdot \frac{v}{c} \cos \hat{\theta}_i \cdot f_c}{\sum_{i=1}^{\hat{N}} \widehat{\mathrm{PG}}_i \cdot G_j^{\omega}\left(\hat{\theta}_i, \hat{\phi}_i\right)}. \tag{9}$$

In order to simplify this equation, we rewrite the azimuth AoA of the ith model MPC as $\hat{\theta}_i = \hat{\boldsymbol{\theta}}_j + \Delta\theta$, where $\Delta\theta$ is the deviation from the model cursor angle $\hat{\boldsymbol{\theta}}_j$. Consistent with the QD model, we also observed from our experiments that diffuse components of a cluster obey a Laplacian distribution, i.e., their path gains decay exponentially with $|\Delta\theta|$ and are distributed symmetrically about $\hat{\boldsymbol{\theta}}_j$. As such, two symmetrical diffuse components (at $\hat{\theta}_i = \hat{\boldsymbol{\theta}}_j + \Delta\theta$ and $\hat{\theta}_i^- = \hat{\boldsymbol{\theta}}_j - \Delta\theta$) will have the same expected path gain $\widehat{\mathrm{PG}}_i = \widehat{\mathrm{PG}}_i^-$ (as well as antenna gain $G_j^{\omega}(\hat{\theta}_i, \hat{\phi}_i) = G_j^{\omega}(\hat{\theta}_i^-, \hat{\phi}_i)$). Then, according to (9), their mean shift is $\frac{\widehat{\mathrm{PG}}_i \cdot G_j^{\omega}(\hat{\theta}_i, \hat{\phi}_i) \cdot \frac{v}{c} [\cos(\hat{\boldsymbol{\theta}}_j + \Delta\theta) + \cos(\hat{\boldsymbol{\theta}}_j - \Delta\theta)] \cdot f_c}{2 \cdot \widehat{\mathrm{PG}}_i \cdot G_j^{\omega}(\hat{\theta}_i, \hat{\phi}_i)} = \frac{v}{c} \cos \hat{\boldsymbol{\theta}}_j \cdot \cos \Delta\theta \cdot f_c \approx \frac{v}{c} \cos \hat{\boldsymbol{\theta}}_j \cdot f_c$. The small-angle approximation holds for $|\Delta\theta| \leq 15^\circ$, as is the case considered here since $\omega \leq 30^\circ$. Applying the same approximation to all $\hat{N}$ model components, it follows that

$$\hat{\mu}_j^{\omega} \approx \frac{v}{c} \cos \hat{\boldsymbol{\theta}}_j \cdot f_c. \tag{10}$$

Notice that the model $\hat{\mu}_j^{\omega}$ is independent of ω. We also confirm this in our experiments, specifically that the measured μ_j^{ω} in (4) varies on average less than 1% across $1^\circ \leq \omega \leq 30^\circ$.

Finally, by substituting into (5)—$\widehat{\mathrm{CV}}_j^{\omega}$ in (7) for CV_j^{ω} and $\hat{\mu}_j^{\omega}$ in (10) for μ_j^{ω}—and rearranging, we get the parameterized model for the absolute Doppler spread

$$\hat{\sigma}_j^{\omega} = \widehat{\mathrm{CV}}_j^{\omega} \cdot \frac{v}{c} |\cos \hat{\boldsymbol{\theta}}_j| \cdot f_c. \tag{11}$$

This equation provides the spread of the dominant beam $\hat{\sigma}_1^{\omega}$ as well as the spread of other beams when they are not interfered by higher-ranking beams. Fig. 6 compares the rank-indexed cumulative distribution function (CDF) between the measured and model spreads. The absolute error between the two averaged over all the measured points is 0.114. Notice the CDFs become progressively flatter with increasing values of j, meaning that lower-ranking cursors will have wider spreads.

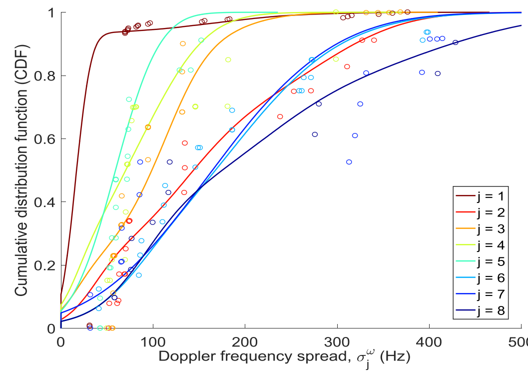

Fig. 6. CDF of measured (circles) and model (lines) Doppler spread for the top eight cursors. For each measured spread in (3), 30 trials of the model spread were generated from (11) using the measured QD parameters. A total of 30 trials were deemed sufficient to average out the stochastic component of the model.

V. Conclusion

In this letter, we provide a parameterized model for Doppler spread in mmWave communication systems. In these systems, transceiver pencilbeams will be steered toward clustered propagation paths in the environment. The key finding is that the spread can be predicted from the relative strength of the dominant path in a cluster with respect to its diffuse paths. Our model was derived from 24 channel acquisitions in an indoor environment for which at most eight clusters were identified and mobility did not exceed 3 km/h. In order to validate the model further, outdoor measurement campaigns at vehicular speed are anticipated in future work.

References

[1] [Online]. Available: http://www.ieee802.org/11/Reports/tgay_update.htm

[2] D. Dupleich, J. Luo, S. Haefner, R. Mueller, C. Schneider, and R. Thomae, “A hybrid polarimetric wide-band beam-former architecture for 5G mm-wave communications,” in *Proc. 20th Int. ITG Workshop Smart Antennas*, Mar. 2016, pp. 1–8.

[3] A. I. Sulyman, A. Alwarafy, G. R. MacCartney, T. S. Rappaport, and A. Alsanie, “Directional radio propagation path loss models for millimeter-wave wireless networks in the 28-, 60-, and 73-GHz bands,” *IEEE Trans. Wireless Commun.*, vol. 10, no. 5, pp. 6939–6947, Jul. 2016.

[4] J.-J. Park, J. Liang, J. Lee, H.-K. Kwon, M.-D. Kim, and B. Park, “Millimeter-wave channel model parameters for urban microcellular environment based on 28 and 38 GHz measurements,” in *Proc. 2016 IEEE 27th Annu. Int. Symp. Personal, Indoor, Mobile Radio Commun.*, Sep. 2016, pp. 1–5.

[5] B. N. Lia and D. G. Michelson, “Characterization of multipath persistence in device-to-device scenarios at 30 GHz,” in *Proc. 2016 IEEE Globecom Workshops*, Dec. 2016, pp. 1–6.

[6] P. B. Papazian, C. Gentile, K. A. Remley, J. Senic, and N. Golmie, “A radio channel sounder for mobile millimeter-wave communications: System implementation and measurement assessment,” *IEEE Trans. Microw. Theory Techn.*, vol. 64, no. 9, pp. 2924–2932, Aug. 2016.

[7] METIS II Project homepage. [Online]. Available: https://metis-ii.5g-ppp.eu/

[8] MiWEBA Project homepage. [Online]. Available: http://www.miweba.eu

[9] mmMAGIC Project homepage. [Online]. Available: https://5g-mmmagic.eu/

[10] A. Maltsev *et al.*, “Quasi-deterministic approach to mm wave channel modeling in a non-stationary environment,” in *Proc. 2016 IEEE Globecom Workshops*, Dec. 2014, pp. 966–971.

[11] S. Wyne, K. Haneda, S. Ranvier, F. Tufvesson, and A. F. Molisch, “Beamforming effects on measured mm-wave channel characteristics,” *IEEE Trans. Wireless Commun.*, vol. 10, no. 11, pp. 3553–3559, Nov. 2011.

[12] A. Malstev, I. Bolotin, A. Lomayev, A. Pudeyev, and M. Danchenko, “User mobility on millimeter-wave system performance,” in *Proc. IEEE Eur. Conf. Antennas Propag.*, Apr. 2016, pp. 1–5.